Phase-Contrast Images

27

CHAPTER PREVIEW

We see phase contrast any time we have more than one beam contributing to the image. In fact, whenever we say "fringes," we are essentially referring to a phase-contrast phenomenon. Although we often distinguish phase and diffraction contrast, this distinction is generally artificial. For example, as we saw in Chapters 23 and 24, even thickness fringes and stacking-fault fringes are phase-contrast images although we usually think of them as two-beam diffraction-contrast images.

Phase-contrast imaging is often thought to be synonymous with high-resolution TEM. In fact, phase contrast appears in most TEM images even at relatively low magnifications. We will draw your attention to its

D. B. Williams et al., *Transmission Electron Microscopy*

role in the formation of moiré patterns and Fresnel contrast at defects. This Fresnel contrast has the same origin as that which we used in Chapter 9 to correct the astigmatism of the objective lens.

As with many of the topics we've discussed, we can approach the problem at several different levels. One danger is that you may be tempted to use one of the prepackaged simulation programs to predict phase-contrast images, without considering the limitations of such packages. We will begin this chapter by discussing some simple approaches to understanding phase-contrast effects as they relate to lattice-fringe imaging.

Phase-Contrast Images

27

27.1. INTRODUCTION

Contrast in TEM images can arise due to the differences in the phase of the electron waves scattered through a thin specimen. This contrast mechanism can be difficult to interpret because it is very sensitive to many factors: the appearance of the image varies with small changes in the thickness, orientation, or scattering factor of the specimen, and variations in the focus or astigmatism of the objective lens. However, its sensitivity is the reason phase contrast can be exploited to image the *atomic structure* of thin specimens. Of course, this also requires a TEM with sufficient resolution to detect contrast variations at atomic dimensions, and the proper control of instrument parameters that affect the phases of the electrons passing through the specimen and the lenses. If you know what you are doing, the procedures can be straightforward; the level of operator skill necessary to obtain such images can be acquired with practice by most TEM users.

The most obvious distinction between phase-contrast imaging and other forms of TEM imaging is the number of beams collected by the objective aperture or an electron detector. As described in the previous chapters, a BF or DF image requires that we select a single beam using the objective aperture. A phase-contrast image requires the selection of *more than one* beam. In general, the more beams collected, the higher the resolution of the image. However, we will see that there are reasons why some beams, which are apparently admitted through the aperture, might not contribute to the image. The details of this process depend on the performance of the electron-optical system. We'll first examine the theory and then consider the practical aspects.

27.2. THE ORIGIN OF LATTICE FRINGES

We can understand the origin of lattice fringes by extending the analysis of Chapter 13 to allow the two beams, **0** and **g**, to interfere, i.e., use the objective aperture to select only two beams. We begin by rewriting equation 13.5

$$\psi = \varphi_0(z)\exp 2\pi i(\mathbf{k}_I \cdot \mathbf{r}) + \varphi_g(z)\exp(2\pi i\mathbf{k}_D \cdot \mathbf{r}) \qquad [27.1]$$

where we know

$$\mathbf{k}_D = \mathbf{k}_I + \mathbf{g} + \mathbf{s}_g = \mathbf{k}_I + \mathbf{g}' \qquad [27.2]$$

We are thus using a two-beam approximation but allowing $\mathbf{s}_g$ to be nonzero. Now we will make some simple substitutions, setting $\varphi_0(z) = A$ and take $e^{2\pi i\mathbf{k}_I \cdot \mathbf{r}}$ out as a factor. We will also represent the expression for φ_g from equation 13.5 as

$$\varphi_g = B\exp i\,\delta \qquad [27.3]$$

where

$$B = \frac{\pi}{\xi_g}\frac{\sin \pi t s_{\text{eff}}}{\pi s_{\text{eff}}} \qquad [27.4]$$

and

$$\delta = \frac{\pi}{2} - \pi t s_{\text{eff}} \qquad [27.5]$$

The $\pi/2$ in the expression for δ takes care of i in equation 13.5 and we'll pretend that the specimen is so thin that we can replace s_{eff} with s. Thus equation 27.1 becomes

$$\psi = \exp(2\pi i\mathbf{k}_I \cdot \mathbf{r})[A + B\exp i(2\pi\mathbf{g}' \cdot \mathbf{r} + \delta)] \qquad [27.6]$$

The intensity can then be expressed as

$$I = A^2 + B^2 + AB[\exp i(2\pi\mathbf{g}' \cdot \mathbf{r} + \delta) + \exp -i(2\pi\mathbf{g}' \cdot \mathbf{r} + \delta)] \qquad [27.7]$$

$$I = A^2 + B^2 + 2AB\cos\left(2\pi\mathbf{g}'\cdot\mathbf{r} + \delta\right) \qquad [27.8]$$

Now $\mathbf{g}'$ is effectively perpendicular to the beam so we'll set it parallel to x and replace δ, giving

$$I = A^2 + B^2 - 2AB\sin\left(2\pi\mathbf{g}'x - \pi st\right) \qquad [27.9]$$

Therefore, the intensity is a sinusoidal oscillation normal to $\mathbf{g}'$, with a periodicity that depends on s and t (just like thickness fringes). (Note that g and s are not bold in equation 27.9 because they represent the magnitude of the vectors, not the vectors themselves.) We can, with care, relate these fringes to the spacing of the lattice planes normal to $\mathbf{g}'$. Although we have obtained this equation using a very simple model, it gives us some useful insight, which will also be helpful when we talk about many-beam images in Chapter 28.

The intensity varies sinusoidally with different periodicities for different values of g'.

This model will be equally valid even if the incident beam is tilted slightly off the optic axis.

27.3. SOME PRACTICAL ASPECTS OF LATTICE FRINGES

27.3.A. If s = 0

If we just have **0** and **g** in the objective aperture and we then set **s** = 0 for reflection G (so $\mathbf{g}' = \mathbf{g}$), we will see fringes in the image (Figure 27.1A) which have a periodicity in the x direction of $1/g$, i.e., the spacing of the planes which give rise to **g**. This result holds wherever **s** = 0, no matter how **0** and **g** are located relative to the optic axis, even if the diffracting planes are not parallel to the optic axis.

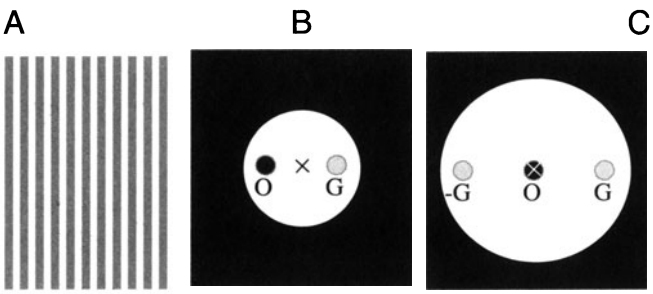

Figure 27.1. (A) Schematic tilted-beam 111 lattice fringes in Si formed using the O and G beams symmetrically displaced relative to the optic axis; **g** is normal to the fringes. (B) Ideal diffraction geometry to produce tilted-beam fringes. (C) On-axis three-beam geometry.

Figure 27.1B shows the ideal geometry for producing images like Figure 27.1A. It is called the "tilted-beam condition" and it means that the planes of interest lie parallel to the optic axis. If we use the geometry shown in Figure 27.1B we have **s** = 0 and the planes are parallel to the optic axis but not parallel to the incident beam. Therefore, the fringes cannot correspond directly to the individual planes. If we use the on-axis geometry shown in Figure 27.1C, the planes are viewed edge on, but **s** ≠ 0 for reflection G; so we must also consider reflection –G.

27.3.B. If s ≠ 0

If the specimen is not exactly flat, then **s** will vary across the image; even if you set **s** = 0 in the DP, it will not be zero everywhere. If **s** is not zero, then the fringes will shift by an amount which depends on both the magnitude of **s** and the value of t, but the periodicity will not change noticeably. We expect this **s** dependence to affect the image when the foil bends slightly, as is often the case for thin specimens. We also expect to see thickness variations in many-beam images, since ideally **s** is not zero for any of the beams; **s** may also vary from beam to beam.

27.4. ON-AXIS LATTICE-FRINGE IMAGING

We've just seen that two beams can interfere to give an image with a periodicity related to $|\Delta\mathbf{g}|^{-1}$. Since one beam is the direct beam, $|\Delta\mathbf{g}|^{-1}$ is just d, the interplanar spacing corresponding to **g**. If you align your beam parallel to a low-index zone axis, then you'll see fringes running in different directions; these fringes in the image must correspond to an array of spots in the DP. The spacings of the spots may be inversely related to the lattice spacings, as shown in Figure 27.2, which extends Figure 27.1 to the many-beam case. In general, this array of spots bears no direct relationship to the *position* of atoms in the crystal.

The trouble is that the fringes look so like atomic planes that you can be easily misled into thinking that they are atomic planes.

We'll see more on this when we discuss image simulation in Chapter 29. In case you are in doubt, compare the beautiful image shown in Figure 27.3A with the projected structure of Si in Figure 27.3B. The Si dumbbells are a pair of atoms which are 1.4 Å apart in this projection of the structure. The aperture used to form the image included 13 reflections, as shown in Figure 27.3C. The diffi-

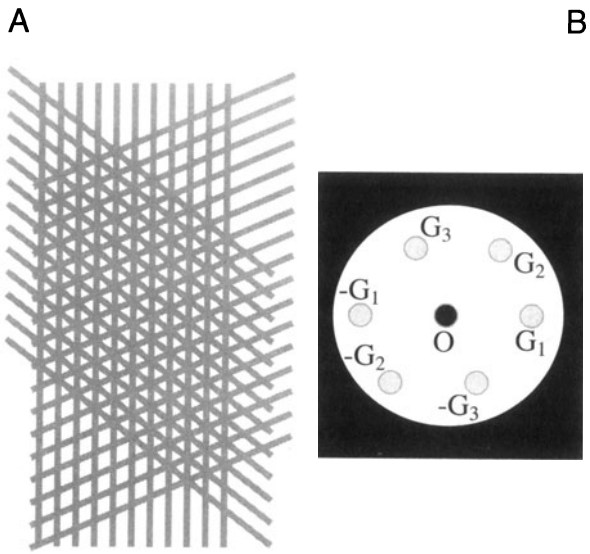

Figure 27.2. (A) Schematic many-beam image showing crossing lattice fringes and (B) the diffraction pattern.

culty is that, in the image, the spots in the dumbbell are really just 1.3 Å apart but the point resolution of the TEM was only ~2.5 Å. You can see from the structure that the real dumbbell spacing corresponds to the (004) plane spacing, but the 004 reflection was *not* used to form the image. The explanation was given by Krivanek and Rez (1980); the dumbbells in the image are caused by the crossing {113} fringes.

The lesson is: we only knew the image did not correspond to the structure because we knew the structure! Taking this example as your guide, consider the case where a defect is present in an image where the perfect-crystal spots are all in the "correct" position. Could you still be certain that the details in the image close to the defect give you a true picture of the location of the atoms close to the defect? The answer is of course "no."

So lattice fringes are *not* direct images of the structure, but just give you lattice spacing information.

On-axis lattice-fringe images are perhaps best used as a measure of the local crystal structure and orientation. The exception, as we'll see in the next chapter, is when these images can only be interpreted using extensive computer simulation. Figure 27.4 illustrates some typical applications of the phase-contrast imaging mode, where we can learn a lot about our material by intuitive interpretation without the need for simulating their images.

Figure 27.4A shows interfaces between a spinel particle and an olivine matrix; Figure 27.4B shows how we

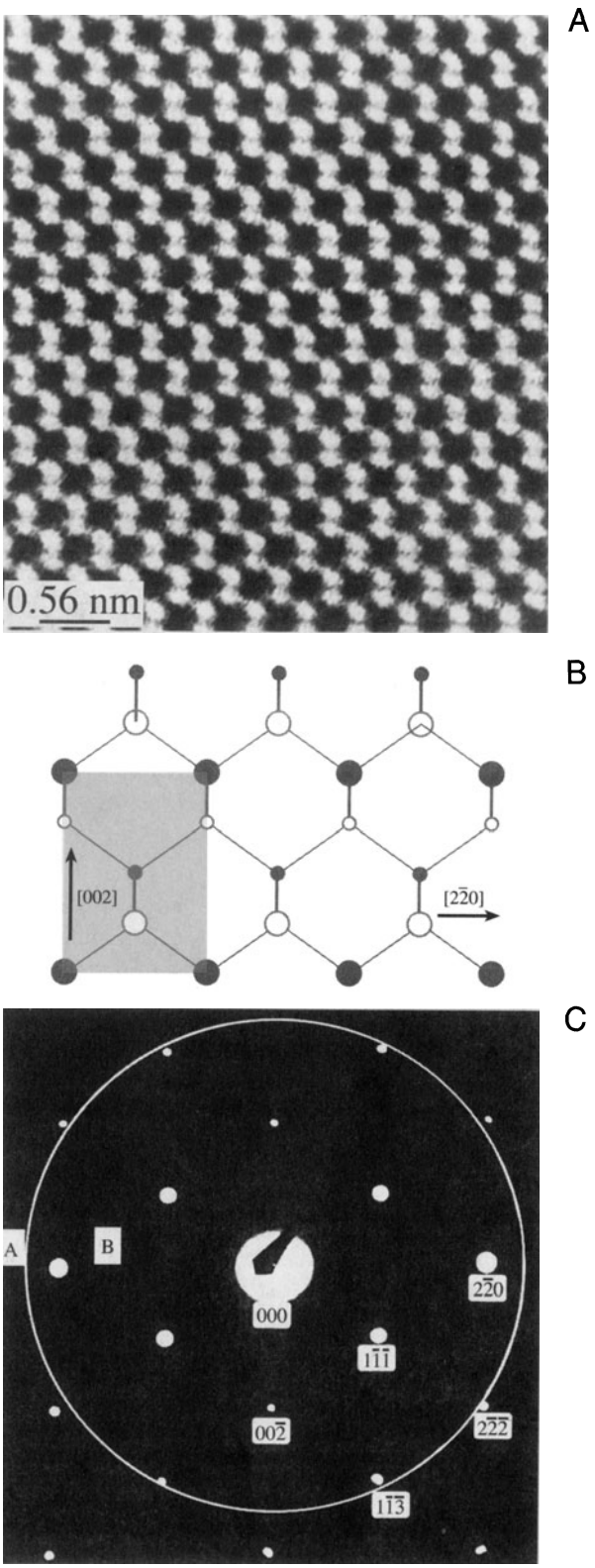

Figure 27.3. (A) On-axis image of a perfect Si crystal; (B) the projected structure; (C) the diffraction pattern showing the 13 spots used to form the image inside the aperture (ring). The Si dumbbells do not correspond to the closely spaced pairs of spots in the image.

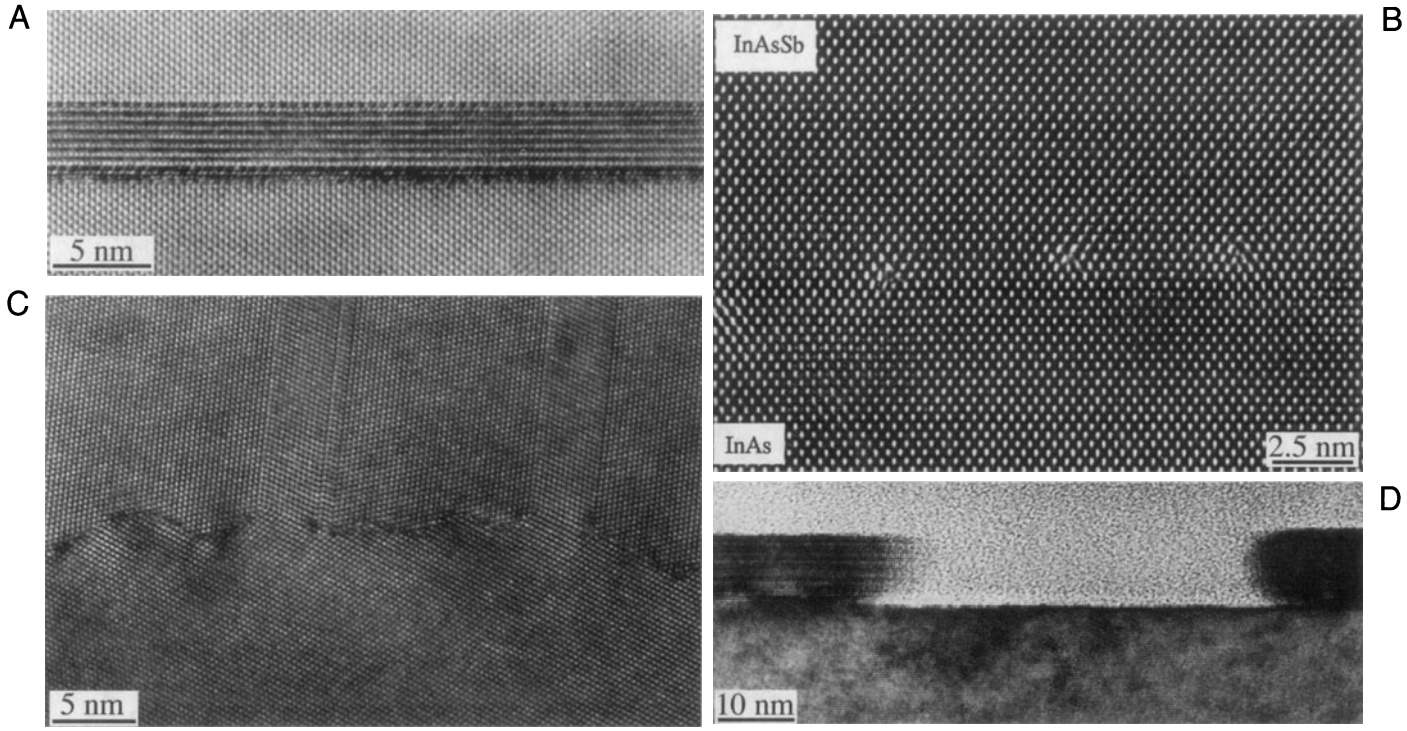

Figure 27.4. Illustrations of lattice images which contain easily interpreted information. (A) The spinel/olivine interface; (B) dislocations at a heterojunction between InAsSb and InAs; (C) a grain boundary in Ge faceting on an atomic scale; (D) a profile view of a faceted surface.

can locate dislocations at a heterojunction; Figure 27.4C shows the atomic-scale faceting of a grain boundary in Ge, and Figure 27.4D illustrates the faceting of a surface.

27.5. MOIRÉ PATTERNS

Moiré (pronounced "mwa-ray") patterns can be formed by interfering two sets of lines which have nearly common periodicities. We can demonstrate two fundamentally different types of interference: the rotational moiré and the translational (often referred to as misfit) moiré. It's easy to understand moirés if you make three transparent sheets of parallel lines (two with the same spacing and one slightly different): you can generate such sets of lines readily using any computer, choosing the line widths to be similar to the gaps between them. Then try these three exercises:

- Take two misfit sets and align them exactly. This gives you a set of moiré fringes which are parallel to the lines forming them, as shown in Figure 27.5A.
- Take two identical sets of lines and rotate them. Now, you produce a set of moiré fringes which is perpendicular to the average direction of the initial lines (Figure 27.5B).
- Take the first two sets and rotate them so you produce moiré fringes, as in Figure 27.5C; but note that their alignment to your reference sets is not obvious.

When the misfit or misorientation is small, the moiré-fringe spacing is clearly much coarser than that of the

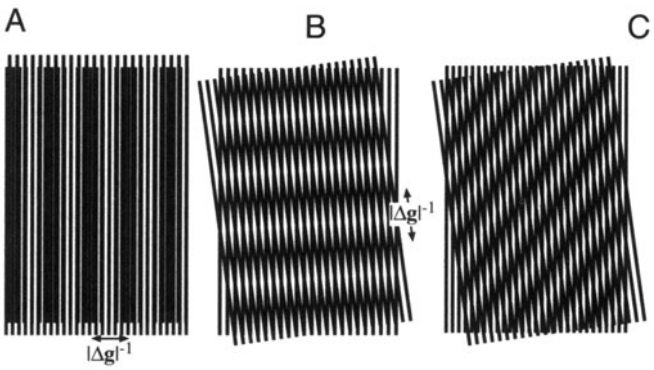

Figure 27.5. (A) Translational moiré fringes; (B) rotational moiré fringes; (C) mixed moiré fringes; note the relationship between the fringes and their constituent lattices.

lines themselves. In particular, if the sets of lines in Figure 27.5 are actually lattice planes in a crystal, the moiré fringes may give information about the crystals even if you cannot resolve the lattice planes. The simplest way to analyze the spacings and orientation of the moiré fringes is to consider the diffraction vectors from the two "lattices." Incidentally, the term "moiré" originated in the textile industry; it's related to the French word for "mohair," the silky hair of the Angora goat; hence the watery or wavy pattern seen in silk fabrics.

27.5.A. Translational Moiré Fringes

In this case, since the planes are parallel, the **g**-vectors will also be parallel. If we write these as $\mathbf{g}_1$ and $\mathbf{g}_2$, we produce a new spacing $\mathbf{g}_{tm}$ given by

$$\mathbf{g}_{tm} = \mathbf{g}_2 - \mathbf{g}_1 \qquad [27.10]$$

As shown in Figure 27.6A (which is from fcc Ni on fcc NiO), we have assigned $\mathbf{g}_2$ to the smaller "lattice" spacing and tm indicates "translational moiré" fringes. The vector $\mathbf{g}_{tm}$ corresponds to a set of fringes with spacing d_{tm}, as shown by the following simple manipulation

$$d_{tm} = \frac{1}{g_{tm}} = \frac{1}{g_2 - g_1} = \frac{\frac{1}{g_2}\cdot\frac{1}{g_1}}{\frac{1}{g_1} - \frac{1}{g_2}} = \frac{d_2 d_1}{d_1 - d_2} = \frac{d_2}{1 - \frac{d_2}{d_1}} \qquad [27.11]$$

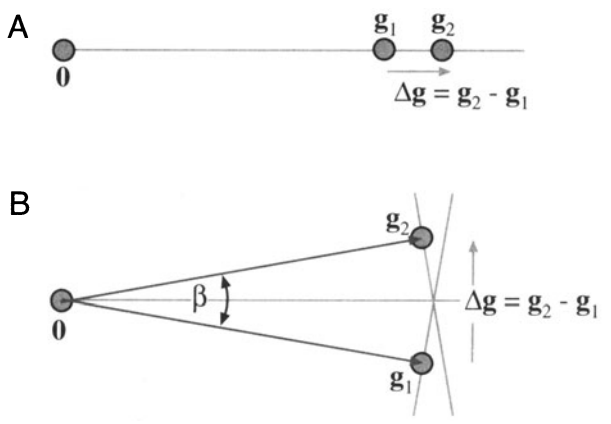

Figure 27.6. (A) Relationship between **g**-vectors for translational moiré fringes; (B) relationship for rotational moiré fringes.

27.5.B. Rotational Moiré Fringes

We follow the same procedure as above, but now the two **g**-vectors are identical in length and rotated through an angle β so that the new **g**-vector, $\mathbf{g}_{rm}$, has length $2g \sin \beta/2$, as shown in Figure 27.6B. The fringe spacing is then

$$d_{rm} = \frac{1}{g_{rm}} = \frac{1}{2g \sin \beta/2} = \frac{d}{2\sin \beta/2} \qquad [27.12]$$

27.5.C. General Moiré Fringes

If we use the same approach to locate $\mathbf{g}_{gm}$ (gm: "general moiré") we can readily show that, for small misorientation, the spacing d_{gm} of our fringes is given by

$$d_{gm} = \frac{d_1 d_2}{\left((d_1 - d_2)^2 + d_1 d_2 \beta^2\right)^{\frac{1}{2}}} \qquad [27.13]$$

27.6. EXPERIMENTAL OBSERVATIONS OF MOIRÉ FRINGES

Moiré fringes in TEM images were first reported early in the history of the microscope. They were used by Minter (1956) to identify a dislocation before lattice imaging was possible. Later, they were regarded as an imaging artifact which obscured the true dislocation structure in twist boundaries. Most recently there has been renewed interest due to the widespread development of thin films grown on different substrates.

You must be wary of the limitation or pitfall of using moiré fringes to learn about interfaces and defects. Moiré patterns result purely from the interference of two "sets of planes." Their appearance will be essentially the same even if the two "crystals" are not in contact.

In TEM the moiré patterns correspond to interference between a pair of beams, $\mathbf{g}_1$ and $\mathbf{g}_2$. If $\mathbf{g}_1$ is generated in the upper crystal and $\mathbf{g}_2$ in the lower, then each reflection $\mathbf{g}_1$ in crystal 1 acts as an incident beam for the lower crystal and produces a "crystal-2 pattern" around each $\mathbf{g}_1$ reflection, as shown in Figure 27.7A. This process is another example of double diffraction as discussed in Section 18.7. Figure 27.7A is from a pair of perfectly aligned but misfitting cubic crystals viewed along their common [001] zone axis; the pattern is indexed in Figure 27.7B. When we have many planes diffracting at a zone axis, as in this pattern, we expect to see crossed moiré fringes.

In the following three sections we will discuss examples of the use of moiré fringes.

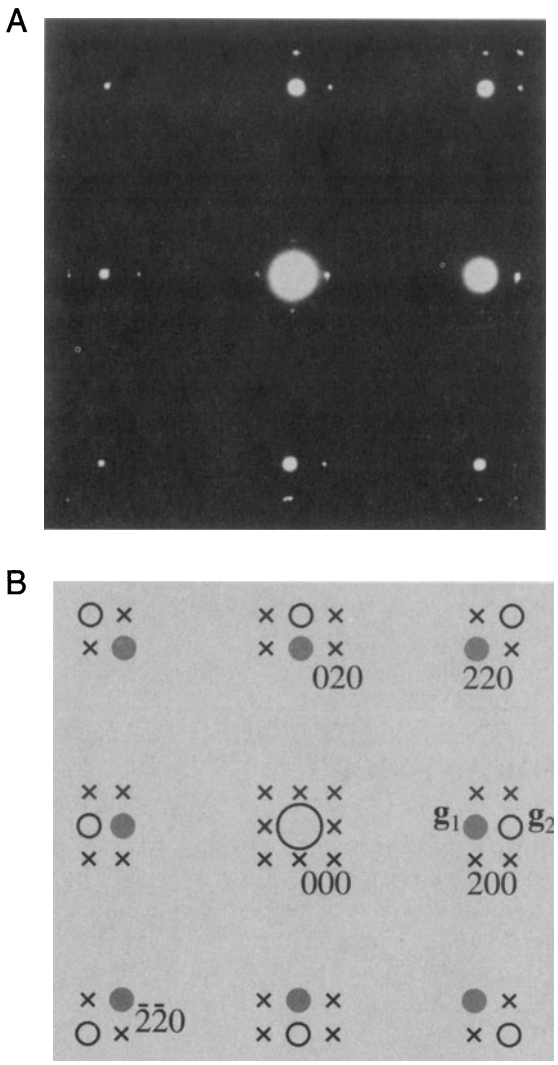

Figure 27.7. (A) Experimental diffraction pattern from perfectly aligned Ni and NiO. Brighter spots are from NiO, which has the larger lattice parameter. (B) Schematic which explains translational moiré fringes. Closed circles ($\mathbf{g}_1$) correspond to crystal 1, open circles ($\mathbf{g}_2$) to crystal 2 and × to double diffraction of $\mathbf{g}_1$ beams by crystal 2. Only × reflections close to $\mathbf{g}_1$ and $\mathbf{g}_2$ have appreciable intensity.

27.6.A. Translational Moiré Patterns

When a continuous film is grown on a thick substrate, one question which is asked is: do the lattice parameters of the thin film correspond to the values of the same material in bulk form? For example, a thin film of a cubic material on a (001) substrate may be tetragonally strained so that the a_{film} lattice parameter is smaller than a_{bulk}, but the c_{film} parameter is larger. If the bulk material has its bulk lattice parameter, then the measurement of d_{tm}, the translational moiré spacing, can give a very accurate value for a_{film}. Furthermore, we can tilt the specimen 45° or 60° and deduce a value for c_{film} to estimate the tetragonal distortion directly.

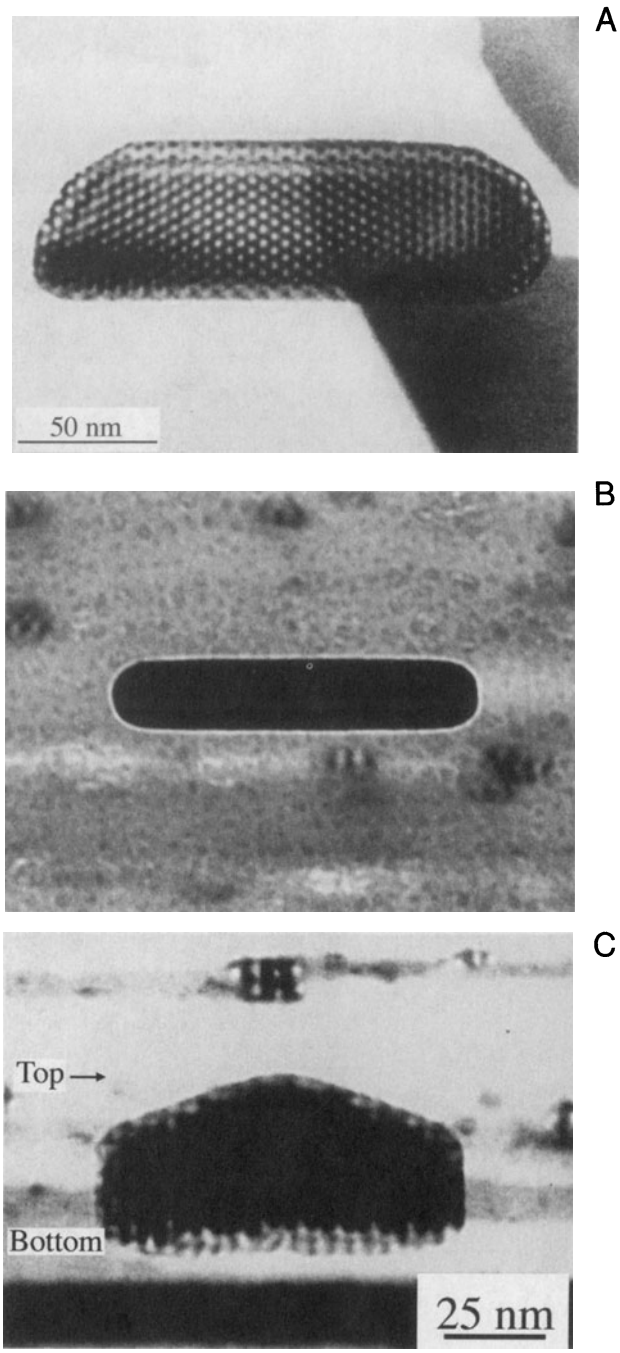

Figure 27.8. (A) The appearance of moiré fringes depends on the thickness of the specimen, as you can see where the edges of this island are inclined relative to the surface of the substrate. (B) The particle is too thick to show moiré fringes when edge on. (C) When this thick particle is tilted over, moiré fringes are seen at both the top and bottom.

Tilting the specimen can also give us information about misfitting islands, as illustrated in Figure 27.8. In this case, we see a hexagonal array of fringes when the two pseudo-hexagonal materials are viewed parallel to their common c-axis. The variation in the contrast of the moiré

fringes around the edge of the particle occurs because the particle facets on inclined planes, as is confirmed when we tilt the specimen. In this system, when the islands are grown on different substrates, they may still grow as platelets. In Figures 27.8B and C the platelet is thick in the direction of the beam but, when tilted over, we again see moiré fringes. In particular, we can see moiré fringes at the *top* of the platelet.

We know that this region is not in contact with the substrate, which reminds us that these fringes do not tell us about the interface structure!

27.6.B. Rotational Moiré Fringes

We often see rotational moiré fringes at twist boundaries, as illustrated for Si in Figure 27.9. A complicating factor is that the misfit may be accommodated by an array of dislocations having a periodicity which is related to the moiré-fringe spacing. The periodic strain field from the dislocations is, of course, only present if the two materials are in intimate contact.

27.6.C. Dislocations and Moiré Fringes

Since the moiré pattern can often be thought of as a magnified view of the "structure" of the materials, such patterns can be used to locate and give information on dislocations which are present in one material but not the other. We can form an image which contains information about the dislocation if it is associated with a terminating lattice plane in one material, but we don't actually "see" the dislocation.

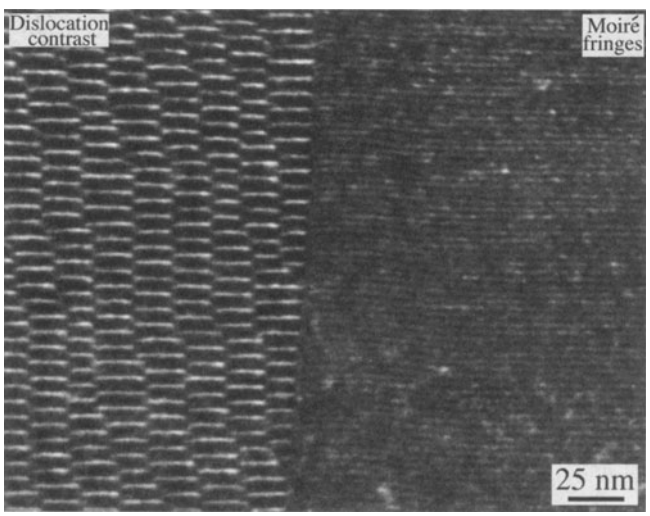

Figure 27.9. WBDF image of moiré fringes at a grain boundary showing very different contrast than the region containing dislocations.

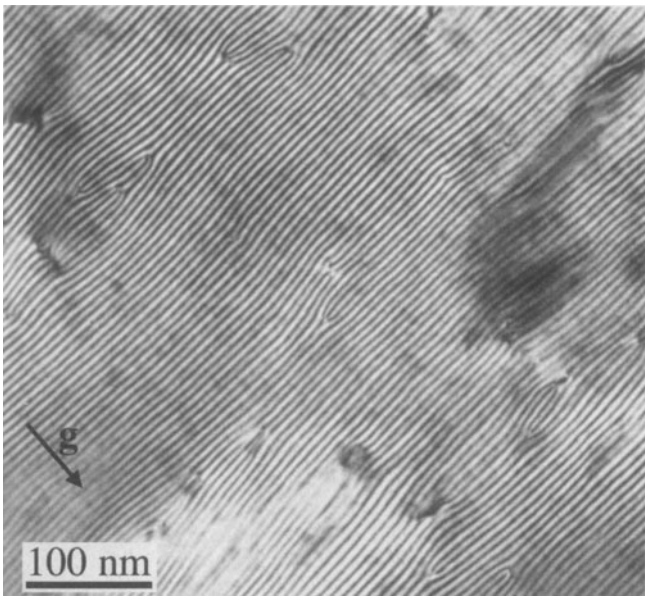

Figure 27.10. Moiré fringes reveal the presence of dislocations in a thin film of CoGa grown on a GaAs substrate. The (001) interface lies parallel to the specimen surface. Although the images contain much detail, most of it cannot readily be related to the structure of the defects.

This effect is illustrated in Figure 27.10; the image appears as a magnified view of the projection of the dislocation. This result can be deceptive, as you can see in Figure 27.11, where we have rotated the perfect grain slightly and changed its spacing.

The images can always be related directly to the projected Burgers vector of the dislocation, but you must know which planes give rise to the fringes. So make some models and experiment.

This analysis even works if you have two or more terminating fringes, but don't put too much emphasis on the actual location of the fringes. Remember, the dislocation may not be parallel to the beam. Moiré fringes may be related to a dislocation in the plane of the interface, since these locally relax the misfit. One example of such an application comes from the work of Vincent (1969), who showed that as Sn islands grew on a thin film of SnTe, the moiré-fringe spacing around the perimeter of the islands gradually increased. Suddenly, the strain at the interface was so large that a dislocation was nucleated to relax the strain and the process began again. The analysis of the changes in moiré-fringe spacing is shown in Figure 27.12.

Since the spacing of moiré fringes essentially gives a magnified view of the misfit between aligned particles and a substrate, we can use them to measure the strain in

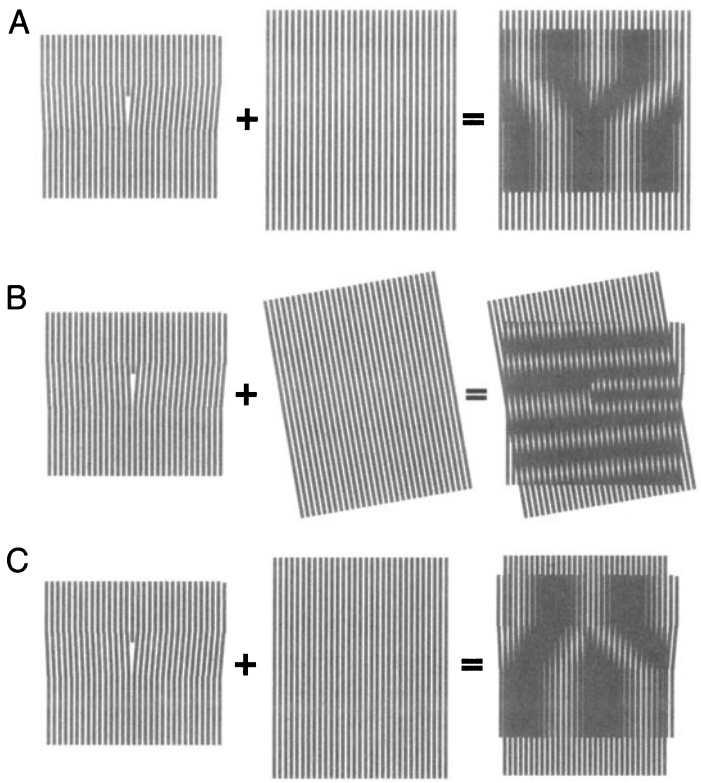

Figure 27.11. Schematic diagrams showing why moiré patterns from regions containing dislocations cannot be readily interpreted: (A) a dislocation image formed by interference between a regular lattice and one containing an extra half plane. (B) In comparison with (A), small rotation of the lattice of either grain can cause a large rotation of the dislocation fringes. (C) A small spacing change of either lattice can cause the dislocation image to reverse.

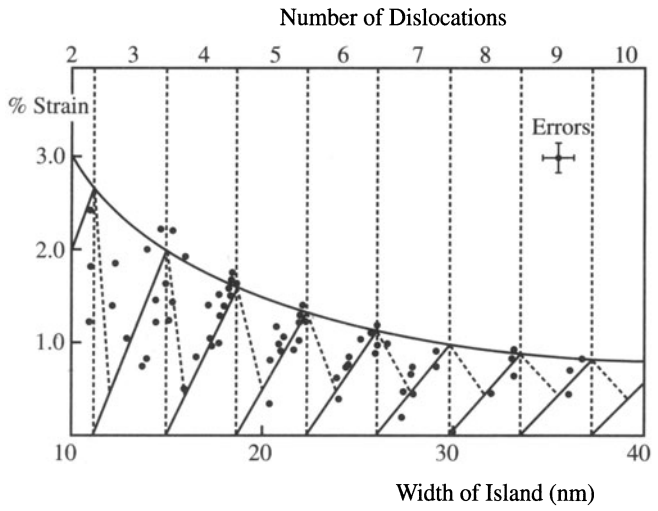

Figure 27.12. Moiré-fringe spacings can be used to monitor the change in lattice parameter as small islands of Sn grow in size on a thin film of SnTe. This plot shows how the strain (measured from the moiré-fringe spacing) can be related to the width of the misfitting island and then to the number of dislocations in the interface.

such particles. In its simplest form, in one dimension, the strain is given by

$$\varepsilon = \frac{a_1 - a_0}{a_0} \qquad [27.14]$$

where a_1 and a_0 are the lattice spacings of the particle and substrate, respectively. You may need to modify this equation if the alignment is not simple cube-on-cube.

27.6.D. Complex Moiré Fringes

Since moiré fringes can occur whenever $\Delta\mathbf{g}$ is small enough to be included in the objective aperture, we can have a situation where the relative rotation is rather large (45° or even 90°) so that $\mathbf{g}_1$ and $\mathbf{g}_2$ correspond to different sets of planes. This is illustrated in Figure 27.13 for YBCO grains rotated 45° on a MgO substrate (Norton and Carter 1995). You can see that, as a bonus, the moiré fringes allow you to locate the 45° boundaries directly. Small rotations of the diffracting planes cause small rotations of $\mathbf{g}$ but large rotations of $\Delta\mathbf{g}$.

Two overlapping lattices produce a pattern of interference fringes which is much coarser than the original pattern and is very sensitive to differences in lattice spacing

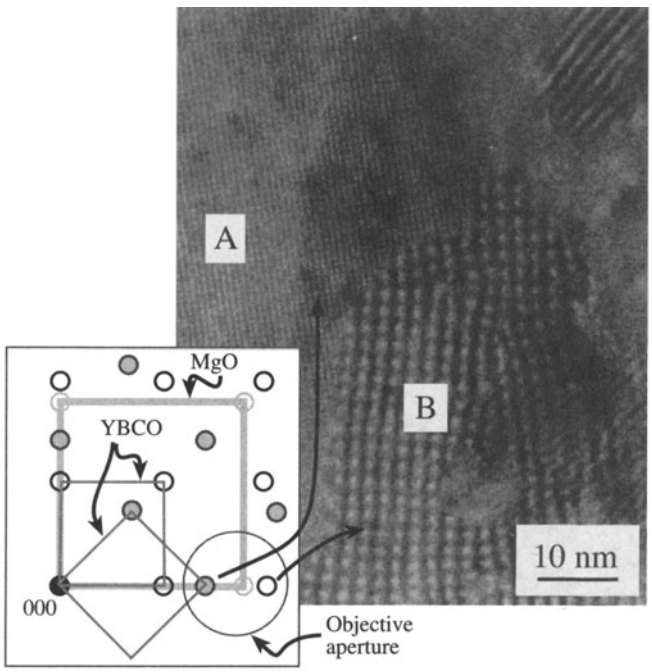

Figure 27.13. Moiré fringes formed when grains of YBCO grown on a single crystal of MgO are aligned to the substrate (B) or rotated through 45°(A); the spacing of the fringes is different so the position of the grain boundary can be identified. The circle in the DP shows the spots that cause the fringes. Small rotations of the fringes away from perfect alignment are exaggerated because the spots are close together.

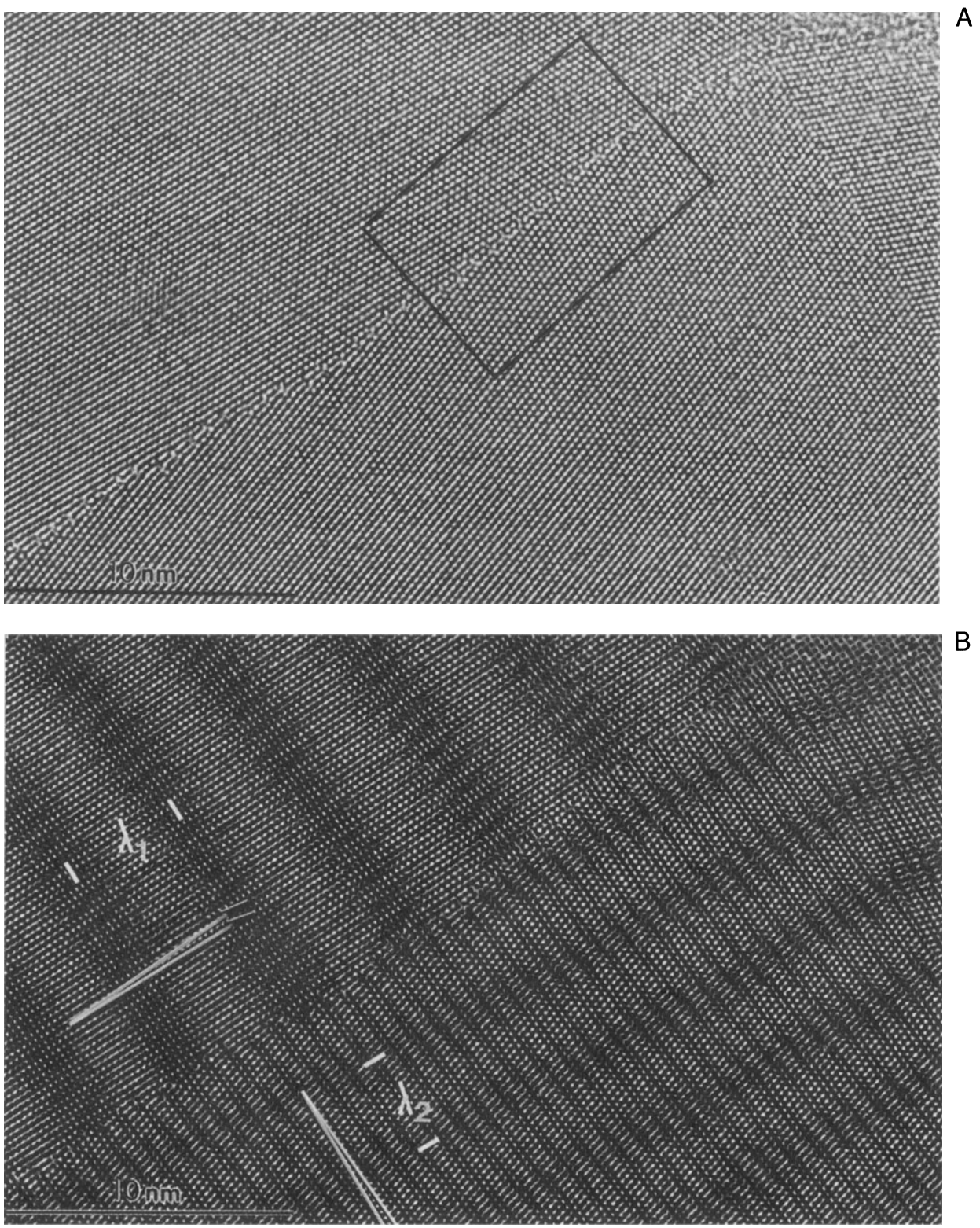

Figure 27.14. The use of "artificial" moiré fringes to analyze a special grain boundary in Al. (A) An experimental image. (B) The same image overlaid with a perfect-crystal lattice transparency, producing moiré fringes of different spacings, λ_1 and λ_2.

and relative orientations. We can use this sensitivity to provide an optical method for examining small rotations or lattice-parameter differences in HRTEM images. Make transparencies of the "distorted" image such as that shown in Figure 27.14A and a reference lattice; the reference lattice could be the perfect-crystal image or a template you have created on the computer. Now overlay the two and rotate/translate them relative to one another. You will have created a new artificial moiré image similar to that shown in Figure 27.14B, which was formed for a special grain boundary in Al by Hetherington and Dahmen (1992). This boundary is special, because one set of {111} planes in the upper grain is nearly normal to one set in the lower grain. How near is near? Hetherington and Dahmen overlapped their experimental image with a template which was drawn to have two sets of lines normal to one another. Overlaying the two images gave moiré fringes which were not quite perpendicular to one another. Careful measurements of the rotation and fringe spacing showed that the fringes in the experimental image were actually 89.3° apart, not 90°.

27.7. FRESNEL CONTRAST

We saw in Chapter 9 that we can use Fresnel-contrast images of holes in carbon films to correct the astigmatism of the objective lens. We'll now discuss how we can use this same contrast mechanism to learn more about particular features in the specimen. In the classical demonstration of Fresnel contrast using visible light, bright fringes can appear in the geometric shadow of an opaque mask, or dark fringes can appear in the illuminated region (e.g., Heavens and Ditchburn 1991). The complication introduced in the TEM version is that the "mask" is not opaque but simply has a different inner potential. Therefore, in any situation where the inner potential changes abruptly, we can produce Fresnel fringes if we image that region out of focus. Since we still focus on a plane which is close to the specimen, we are in the near-field or Fresnel regime. Now we extend this concept and say that

> Whenever we observe contrast only because we are forming an out-of-focus image, we are forming a Fresnel image.

Since we often study lines, planes, or platelets by this technique, we'll often see Fresnel fringes.

27.7.A. The Fresnel Biprism

We can demonstrate a particularly simple interference phenomenon by placing a wire at a position F on the optic axis, as shown in Figure 27.15A. Since the beam is narrow, the wire should be less than 1 μm in diameter and can be made of a drawn glass fiber coated with Cr or Au. If we apply ~10 V to the wire, it will bend the electron beam on either side in opposite directions. The resulting interference fringes can be recorded on a photographic film, as shown in Figure 27.15B. The wire here is acting as a beam splitter; we'll encounter it again when we discuss holography in Chapter 31. The visible-light analog is the prism. Notice how the wire acts to produce two virtual sources s_1 and s_2, which are D_s apart. Horiuchi (1994) gives the following equation to define a measure of the degree of spatial coherence, γ, which, as we discussed in Section 5.2 and Figure 5.13, is a function of the source size. Horuchi shows that

$$\gamma = \frac{I_{Max} - I_{Min}}{I_{Max} + I_{Min}} \qquad [27.15]$$

where I_{Max} is the intensity of the central fringe and I_{Min} is the intensity of the first minimum in Figure 27.15B.

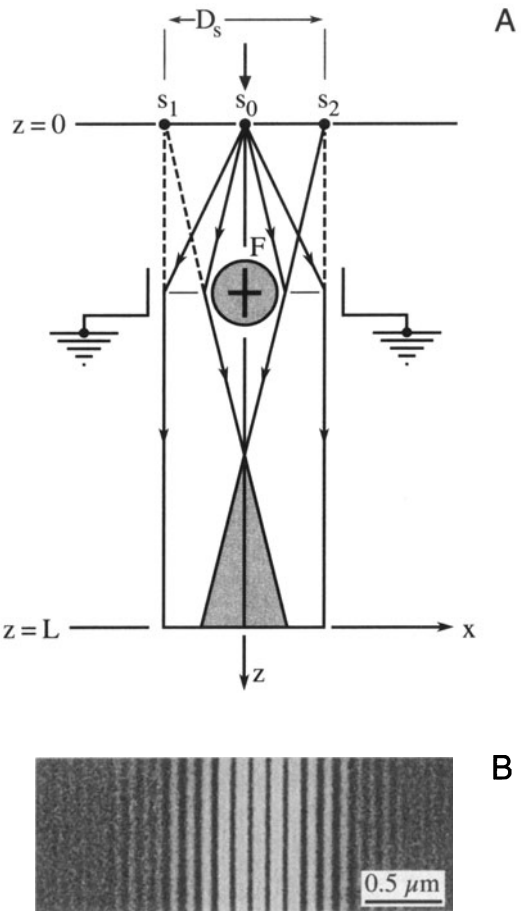

Figure 27.15. (A) A Fresnel biprism formed using a charged wire placed in the path of the beam; (B) the resulting interference fringes in the image.

27.7.B. Magnetic-Domain Walls

Although we'll discuss imaging magnetic materials in Chapter 31, it is appropriate here to consider briefly the similarity of Lorentz microscopy of magnetic-domain walls to other interference images. We know from our discussion of magnetic fields in the electron lens, in Chapter 6, that the Lorentz force on an electron with velocity **v** is proportional to **v**×**B**. If the sign of **B** is opposite in two adjacent domains, then the electrons will be deflected in opposite directions, as shown in Figure 27.16. The "converging" domain wall is remarkably similar to the electron interferometer. We can indeed produce a series of interference fringes. You should consult the original analysis of Boersch *et al.* (1960), but the basics are given by Hirsch *et al.* (1977) who show that the fringe spacing Δx is given by

$$\Delta x = \frac{\lambda(L + \ell)}{2\ell\beta_m} \qquad [27.16]$$

where β_m is the angle of deflection of the beam, λ is the electron wavelength, ℓ is the "source"-to-specimen distance, and L is the specimen-to-"detector" distance. Quotation marks are used to emphasize that these are "effective" distances like the "camera length." The value of Δx can be ~20 nm. You'll only see such interference fringes if you form the image using parallel illumination. We'll return to magnetic imaging in Chapter 31.

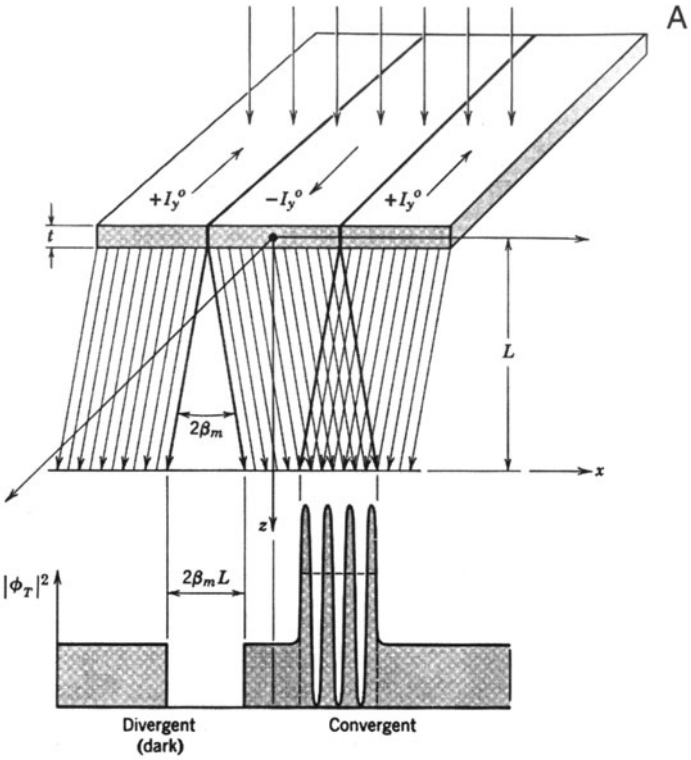

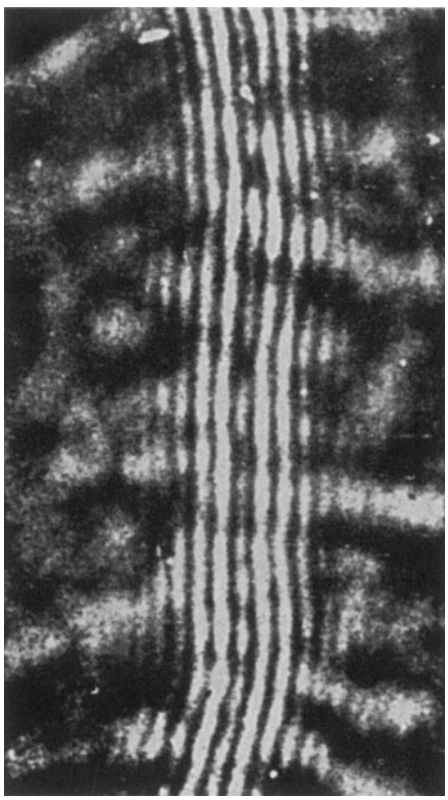

Figure 27.16. (A) Deflection of the electron beam by magnetic-domain walls; compare with Figure 27.15A. (B) Interference fringes from one such wall; compare with Figure 27.15B.

27.8. FRESNEL CONTRAST FROM VOIDS OR GAS BUBBLES

You might think that it would be difficult to image voids or small gas-filled cavities when there is no associated strain field, because voids or cavities do not scatter electrons. However, we can image holes which are fully enclosed inside the specimen by defocusing the image and observing the special form of phase contrast termed Fresnel contrast, which we introduced back in Sections 2.9 and 9.5. In principle, we can apply this technique to holes which contain a liquid or even a solid (i.e., a second phase). In the latter case, however, the Fresnel contrast is likely to be hidden by strain contrast in the specimen.

You can image small voids or gas bubbles in two ways:

- By orienting the region of interest so that **s** = 0; the cavity then reduces the "thickness" of material locally.
- By using Fresnel contrast, as explained by Wilkens (1975).

In the Fresnel technique, the image shows contrast whenever the objective lens is not focused on the bottom surface of the specimen.

Fresnel-contrast images are always out of focus.

Wilkens expresses the wave function as

$$\psi(t, \mathbf{r}') = \psi_0(t)[1 + \Delta_r(\mathbf{r}') + i\Delta_i(\mathbf{r}')] \quad [27.17]$$

Here, $\psi_0(t)$ is the wave function in the absence of the cavity; Δ_r and Δ_i are real functions which depend on:

- The location and dimensions of the cavity.
- The extinction distance and absorption parameter of the matrix (ξ_g and ξ_g').
- The potential difference, ΔV, between the inner potential of the matrix, V_0, and that of the cavity, V_c (it could be filled or empty).

In the case of thick foils where z_c, the size of the cavity in the direction of the beam, is $< 0.1\xi_g$, the wave function can be expressed as

$$\psi(t, \mathbf{r}') = \psi(t)[1 + i\Delta_i(\mathbf{r}')] \quad [27.18]$$

where Δ_i (using $w = s\xi_g$) is given by

$$\Delta_i = -\left(2\varepsilon_0 - \frac{1}{\xi_g}\frac{1}{(1+w)^{1/2}}\right) z_c(\mathbf{r}')p_i(z) \quad [27.19]$$

The difference in inner potential is included in ε_0, which is defined by the equation

$$\varepsilon_0 = -\frac{\Delta V}{E}k \quad [27.20]$$

Here, k is the magnitude of the wave vector and E is the energy of the electron beam. When the thickness dependence is damped out (the foil is thick), the intensity can be expressed quite simply as

$$|\psi(t, \mathbf{r}')|^2 = |\psi_0(t)|^2\left(1 + \Delta_i^2\right) \quad [27.21]$$

We can summarize some results from this study:

- When the image is in focus, the cavity is invisible so you have to view it out of focus to observe the Fresnel-fringe contrast.
- The contrast depends on the difference in the inner potential of the matrix and the cavity; we usually see the most contrast if the content of the cavity is vacuum, because then ε_0 is greatest.

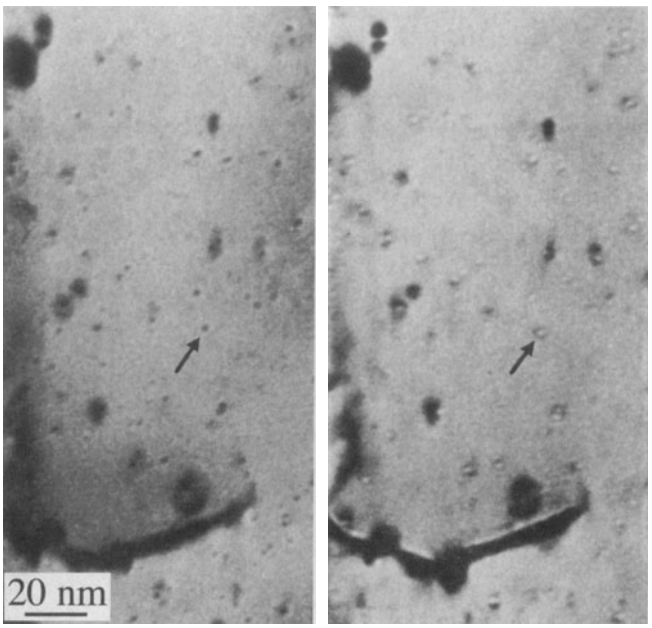

Figure 27.17. Fresnel contrast from He bubbles in Au. (A) Overfocus image. (B) Underfocus image.

- The contrast does depend on the wavelength of the electrons through both k and E.
- Cavities as small as 1–2 nm in diameter can be imaged using Δf values of 0.5 to 1.0 μm.
- In the case where $w = 0$ and $2\varepsilon_0 > \xi_g^{-1}$ (so Δ_i is < 0), if $\Delta f < 0$, the image is a bright dot surrounded by a dark fringe; if $\Delta f > 0$, the dot is dark and the fringe is bright.
- This is the same behavior as we saw in Figure 9.20, where we had a dark fringe at underfocus and a bright fringe at overfocus.

The contrast is illustrated in Figure 27.17. You should note that it is not the same as the black–white contrast from small precipitates discussed in Chapter 25. You'll find a more detailed analysis in the article by Rühle and Wilkens (1975).

27.9. FRESNEL CONTRAST FROM LATTICE DEFECTS

This topic is one which is receiving more attention as the computer and simulation programs become, respectively, more powerful and more user-friendly. The reason for this increased attention is clear, as Bursill *et al.* (1978) showed in their pioneering studying of Fresnel fringes from edge-on defects. They demonstrated that, if you take great care in determining all the electron optical parameters (particu-

larly what defocus steps you are using), you can obtain new information on edge-on defects. The defect images are very sensitive to the model used to simulate them, but you will need other information for a full analysis. We'll refer you to their paper on the {100} platelets in diamond and concentrate on two more widely applicable situations, namely, end-on dislocations and edge-on grain boundaries; in both cases we now have many techniques, such as XEDS, EELS, and HRTEM, to complement the Fresnel-fringe studies.

27.9.A. Grain Boundaries

We might expect almost any grain boundary to show a localized change in the inner potential. However, following the original suggestion by Clarke (1979), Fresnel-contrast imaging has been used most extensively to study those interfaces which are thought to contain a thin layer of glass (Clarke 1979, Ness *et al.* 1986, Rasmussen *et al.* 1989, Rasmussen and Carter 1990). Part of the reason for this emphasis is simply that other techniques tend to give ambiguous results for such interfaces (Simpson *et al.* 1986).

When you use the Fresnel-fringe technique to study grain boundaries or analyze intergranular films, you must orient the boundary in the edge-on position so that you can probe the potential at the boundary. Later, in Section 29.11, we will consider the actual shape of this "potential well."

In a real TEM specimen, the grain boundary is likely to change in thickness even if only by a nanometer or so. Since the specimen will be quite thin, this change can give an appreciable contribution to the difference in the "effective inner potential" seen by the electron beam. You can defocus the image to see the Fresnel contrast shown in Figure 27.18.

The Fresnel-contrast technique can equally well be applied to phase boundaries, with perhaps the most thoroughly studied example being the Si/SiO_2 interface (Taftø *et al.* 1986, Ross and Stobbs 1991a). Since the details of the contrast are sensitive to the abruptness of the change in the inner potential, the technique can also produce information on this aspect of the interface (Ross and Stobbs 1991b). Nevertheless, you must always look for associated changes in the real geometry which can even occur when you're just forming Fresnel fringes from the edge of the specimen (Fukushima *et al.* 1974).

27.9.B. End-On Dislocations

We've just seen that we can detect Fresnel-fringe contrast from edge-on high-angle grain boundaries. We might then ask: is it possible to detect similar contrast from low-angle grain boundaries, i.e., grain boundaries which consist of arrays of distinct dislocations? It is indeed possible, as shown in the series of images from a tilt boundary in NiO

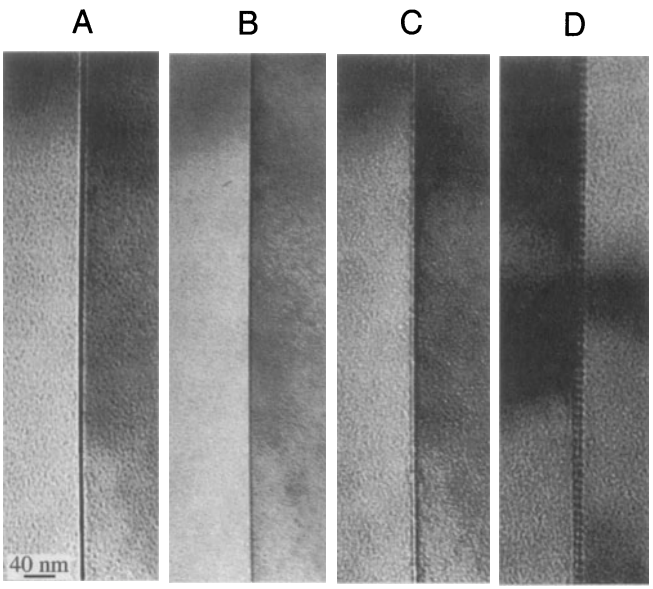

Figure 27.18. (A–D) A through-focus series of images from an edge-on GB showing the changes in Fresnel contrast. The image in (D) shows the boundary tilted over to reveal its periodic structure more clearly.

in Figure 27.19. Rühle and Sass (1984) analyzed this through-focus series, and images of other grain boundaries, by assuming that there is a change in $\Delta V(\mathbf{r})$ in the mean inner potential at the core of the dislocation. They proposed two models for $\Delta V(\mathbf{r})$. In model 1, when $r < r_0$

$$\Delta V(\mathbf{r}) = \Delta V_0 \left\{ 1 - e^{\frac{-(r - r_0)}{a}} \right\} \qquad [27.22]$$

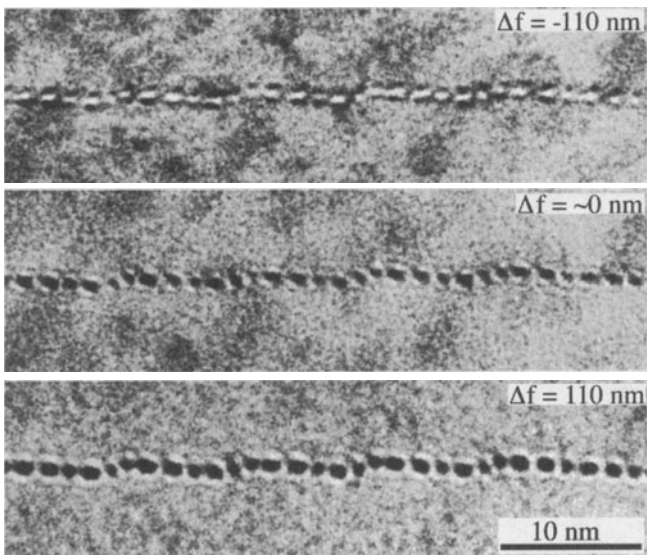

Figure 27.19. Series of experimental images recorded at different values of Δf for a low-angle grain boundary in NiO. Each white or black spot corresponds to one end-on dislocation.

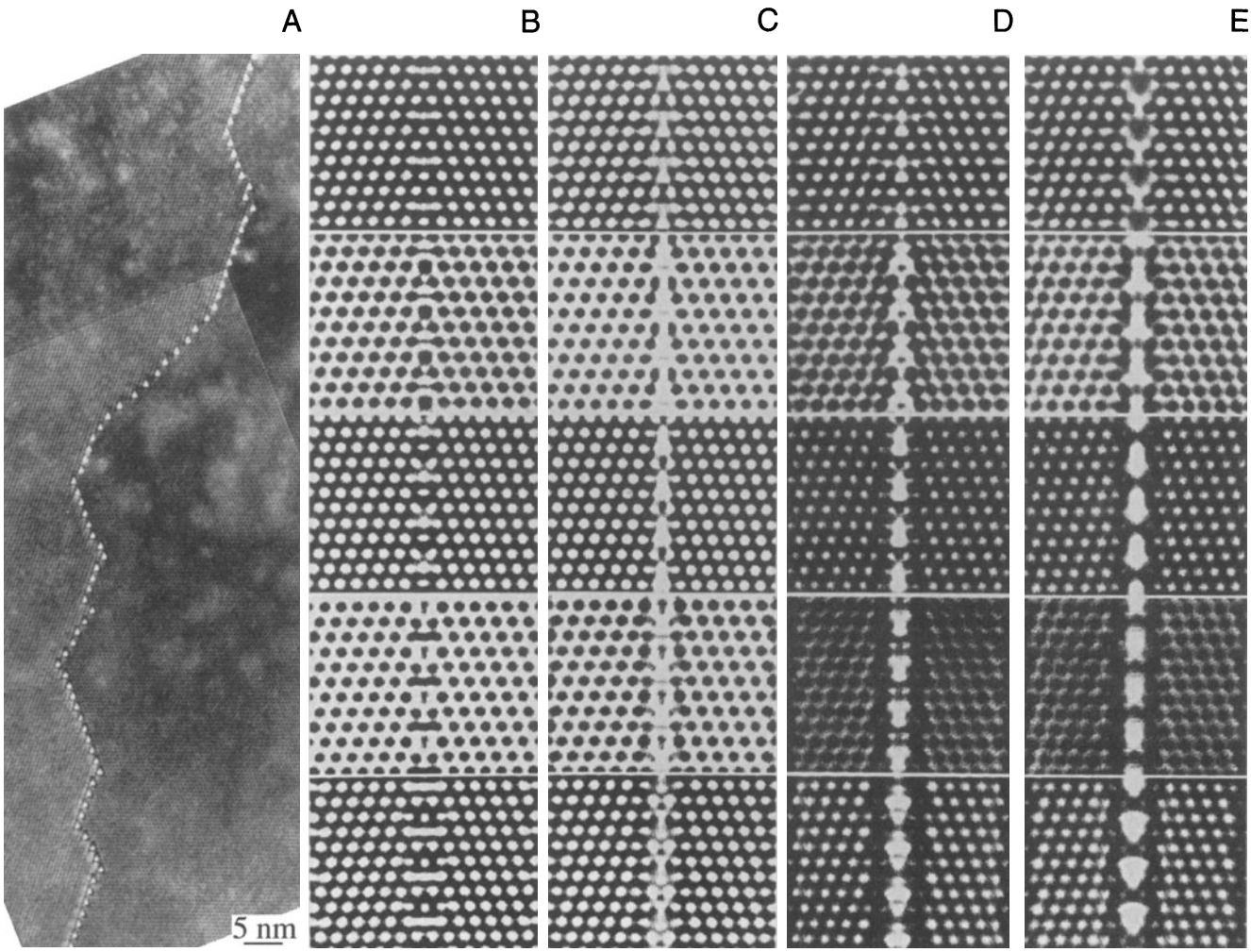

Figure 27.20. The structure of the (112) lateral twin boundary in a thin-foil of spinel consists of triangular prisms with a density lower than the bulk crystal. (A) Fresnel contrast is seen when these prism-like defects are imaged out of focus. (B–E) Simulated images; each column is a different model: (B) no ions removed, (C) ion sites in the prisms half occupied, (D,E) all ions removed. The defocus in each row increases from the top (–10 nm, –70 nm, –130 nm, –160 nm, –210 nm), and the thickness is 5.7 nm.

but when $r > r_0$

$$\Delta V(\mathbf{r}) = 0 \qquad [27.23]$$

The constant a is ~ $0.1r_0$. In model 2

$$\Delta V(\mathbf{r}) = \Delta V_0 \exp\left(-r^2/r_0^2\right) \qquad [27.24]$$

In both cases, ΔV_0 is negative. As an example of the quantities involved in these equations, if the Burgers vector of the dislocations is [110], Rühle and Sass found that $\Delta V_0 = 0.09V_0$ for $r_0 = 3.2$ Å. They could not distinguish between the two models for $\Delta V(\mathbf{r})$, but two clear points come out of this study:

- You must know the inclination of your foil surface. If the lower surface is inclined to the horizontal, then thicker parts of the specimen can be much closer to the objective lens than in the thin area; you can do a quick calculation to prove this point.
- The inner potential at a dislocation core is different than the bulk value. You should expect the value of ΔV_0 to be influenced by a change in stoichiometry or impurity segregation.

Before leaving this topic we should point out that the inner potential at the grain boundary may not be uniform, perhaps because the width of the interface varies or the interface facets on a mesoscopic scale. Even then, you can still

see Fresnel effects which relate to the periodicity in the grain boundary even if this periodicity is not associated with dislocations. A particularly clear example of such a variation is shown in Figure 27.20, where a twin boundary in spinel is essentially constructed of parallel triangular tubes; the inner potential inside the tube is much lower than the matrix value and the tubes are only about 1.2 nm high (Carter *et al.* 1987).

CHAPTER SUMMARY

Phase contrast will occur whenever we have more than one beam contributing to the image. The clue is: if you see fringes of any sort, then you are almost certainly observing a phase-contrast image. This conclusion even applies to stacking-fault fringes (Chapter 24) and thickness fringes (Chapter 23) in what are traditionally called two-beam diffraction-contrast images.

Phase-contrast images are widely used in three forms:

- Images which relate directly to the structural periodicity of the crystalline specimen.
- Moiré-fringe images.
- Fresnel-contrast images.

It is even possible for an image to show all three effects at the same time. So you must remember that phase-contrast effects don't just occur when you are forming high-resolution images. You will create Fresnel contrast whenever your specimen is thick or you are working out of focus. You should note that it is difficult, but not impossible, to be quantitative in your analysis of Fresnel fringes.

The usefulness of moiré fringes continues to surprise even experienced users of the TEM. However, you still have to exercise caution when interpreting what they are telling you about defects in your material.

The appearance of the Fresnel image varies with small changes in the thickness, orientation, or scattering factor of your specimen, and variations in the focus or astigmatism of the objective lens.

REFERENCES

Specific References

Boersch, H., Hamisch, H., Wohlleben, D., and Grohmann, K. (1960) *Z. Phys.* **167**, 72.

Bursill, L.A., Barry, J.C., and Hudson, P.R.W. (1978) *Phil. Mag.* **A37**, 789.

Carter, C.B., Elgat, Z., and Shaw, T.M. (1987) *Phil. Mag.* **55**, 1.

Clarke, D.R. (1979) *Ultramicroscopy* **4**, 33.

Fukushima, K., Kawakatzu, H., and Fukami, A. (1974) *J. Phys.* **D7**, 257.

Heavens, O.S. and Ditchburn, R.W. (1991) *Insight into Optics,* p. 73, John Wiley & Sons, New York.

Hetherington, C.J.D. and Dahmen, U. (1992) *Scanning Microscopy Supplement* **6**, p. 405, Scanning Microscopy International, AMF O'Hare, Illinois.

Hirsch, P.B., Howie, A., Nicholson, R.B., Pashley, D.W., and Whelan, M.J. (1977) *Electron Microscopy of Thin Crystals,* 2nd edition, Krieger, Huntington, New York.

Horiuchi, S. (1994) *Fundamentals of High-Resolution Transmission Electron Microscopy,* North-Holland, Amsterdam.

Krivanek, O.L. and Rez, P. (1980) Proc. 38th Ann. EMSA Meeting (Ed. G.W. Bailey), p. 170, Claitors, Baton Rouge, Louisiana.

Minter, J.W. (1956) *Proc. Roy. Soc.* (London) **A236**, 119.

Ness, J.N., Stobbs, W.M., and Page, T.F. (1986) *Phil. Mag.* **54**, 679.

Norton, M.G. and Carter, C.B. (1995) *J. Mater. Sci.* **30**, 381.

Rasmussen, D.R. and Carter, C.B. (1990) *Ultramicroscopy* **32**, 337.

Rasmussen, D.R., Simpson, Y.K., Kilaas, R., and Carter, C.B. (1989) *Ultramicroscopy* **30**, 52.

Ross, F.M. and Stobbs, W.M. (1991a) *Phil. Mag.* **A63**, 1.

Ross, F.M. and Stobbs, W.M. (1991b) *Phil. Mag.* **A63**, 37.

Rühle, M. and Sass, S.L. (1984) *Phil. Mag.* **A49**, 759.

Rühle, M. and Wilkens, M. (1975) *Crystal Lattice Defects* **6**, 129.

Simpson, Y.K., Carter, C.B., Morrissey, K.J., Angelini, P., and Bentley, J. (1986) *J. Mater. Sci.* **21**, 2689.

Taftø, J., Jones, R.H., and Heald, S.M. (1986) *J. Appl. Phys.* **60**, 4316.

Vincent, R. (1969) *Phil. Mag.* **19**, 1127.

Wilkens, M. (1975) in *Electron Microscopy in Materials Science,* **II** (Eds. U. Valdrè and E. Ruedl), p. 647, CEC, Brussels.